JOURNAL OF THERMOPHYSICS AND HEAT TRANSFER
Vol. 18, No. 4, October–December 2004

Adaptive Surface Microprofiling for Microfluidic Energy Conversion

G. F. Naterer*
University of Manitoba, Winnipeg, Manitoba R3T 2N2, Canada

Adaptive microprofiling is a newly proposed technique of embedding open microchannels within a surface to take advantage of resulting slip-flow behavior and drag reduction. The objective of this paper is to predict the optimal geometrical profiles of such microchannels, particularly for minimizing entropy production in convective heat-transfer problems. A theoretical slip-flow formulation (within microchannels) is developed for Knudsen numbers between about 0.02 and 0.07. These values fall within the range governed by the Navier–Stokes equations with slip-flow boundary conditions. Numerical results show that a fourth-order geometrical profile yields lower entropy production than a linearly diverging microchannel. With rapid advances in micromachining technology, it is viewed that adaptive microprofiling can become a useful alternative technique of drag reduction, while increasing heat-transfer effectiveness. These combined objectives can be realized through the newly formulated approach with entropy-based microprofiling, which establishes the optimal microgroove patterns by minimizing entropy production over the surface.

Nomenclature

d	=	depth of microchannel, m
K_1	=	slip coefficient
Kn	=	Knudsen number (mean free path divided by characteristic length scale)
k	=	thermal conductivity, W/mK
L	=	length of plate, m
n	=	number of microchannels
q'	=	heat flow per unit length, W/m
Re	=	Reynolds number
T	=	temperature, K
u	=	freestream velocity
W	=	width of plate, m
W_s	=	width of microchannel, m
ζ	=	surface parameter, d/W
λ	=	surface parameter, $(W_s + 2d)/W$
μ	=	dynamic viscosity, kg/ms
ϕ	=	irreversibility distribution ratio

Subscripts

w	=	wall
∞	=	ambient (freestream) value

I. Introduction

RATHER than mainly reducing the size of microdevices (a common goal in microelectronics), recent advances in microfluidics technology have focused on more sophisticated energy and fluid transport capabilities. These capabilities range from chemical separation in biotechnology applications to controlled surface roughness in aerodynamics and heat exchangers. This paper investigates a new application and drag-reduction technique of embedded microchannels within surfaces. These open microchannels can simultaneously reduce surface friction and raise heat-transfer capabilities by minimizing the net entropy production over the surface.

Received 2 March 2004; revision received 16 May 2004; accepted for publication 17 May 2004.

*Professor, Department of Mechanical and Manufacturing Engineering, 15 Gillson Street. Member AIAA.

Recently developed experimental methods, such as micro particle image velocimetry (PIV) and confocal microscopy, have made it possible to understand various processes arising in microchannel flows. In particular, fluorescence confocal microscopy is a useful experimental technique for investigating diffusive mixing in microfluidic applications. For example, it can be used to measure interfacial transport in convection problems involving mixing of adjacent fluid streams. A confocal microscope can outline the detailed shape of a diffusively mixed region between streams of fluids containing molecules, as they become fluorescent when they react with each other. Based on the width and growth of the intermixed region, the diffusive mixing rate can be determined. This paper investigates diffusion in boundary-layer flow with adjacent slip-flow (within open microchannels) and no-slip regions (outside microchannels).

Recent microfluidic developments have allowed miniscule quantities of liquid to be transported through networked channels. Flow rates can be controlled by micromechanical or electrohydrodynamical pumping, electro-osmotic methods, electrowetting, or thermocapillary pumping.[1] Kataoka and Troian[2] outline a novel technique of driving microfluidic motion, based on applied temperature gradients across a selectively patterned surface. The surface consists of alternating stripes of bare and coated SiO_2. Liquid flow is manipulated by simultaneously applying a varying thermal pattern at the liquid–solid interface and a shear stress at the air–liquid interface.

Past studies have developed multidimensional numerical methods for both slip-flow and no-slip conditions in microchannel flows.[3] Subsonic flow of helium through microchannels with varying aspect ratios was studied by Raju and Roy.[3] Although predicted mass flow rates agreed with experimental data within about ±8% at low Knudsen numbers, significant variations are noticed in a free-molecule case involving an exit Knudsen number of 17.72. In that case, wall boundary conditions exhibit a large effect on numerical predictions. Reducing the momentum accommodation coefficient for the slip-flow boundary conditions yields closer agreement with mass flow rate and specific impulse predictions obtained previously with direct simulation Monte Carlo.

Because of microdevice constraints, it is often desirable to reduce the frictional pressure drop in microchannel flows. Lim and Choi[4] design optimally curved microchannels based on a gradient method and iterative modifications of an initially circular shape. Reynolds numbers of 0.1, 1, and 10 were studied for 90- and 180-deg curved channels. It was observed that shape optimization could reduce the pressure drop by up to about 20%. Other similar microchannel geometries, such as a microcolumn with two 90-deg bends,[5] have practical applications in microfluidic devices requiring a longer contact length within a compact area. Similar to this shape optimization,

this paper considers optimal microprofiling of a surface to minimize entropy production. This can reduce the frictional pressure drop, while transferring a specified heat flow from the surface to the fluid. Unlike past methods of modeling surface roughness by an effective friction factor, the new method develops approximate analytical solutions for the embedded microchannels to give more rigorously optimized surface characteristics.

In contrast to the conservation equations for microfluidic transport, the Second Law involves an inequality and a thermodynamic state variable that cannot be measured directly (entropy). Dincer and Rosen[6] characterize the performance of thermal energy storage systems using exergy. Because exergy losses can be represented directly in units of watts, the costs associated with system inefficiencies can be more readily calculated than entropy production values. Reducing entropy production in heat-exchange processes can be achieved through equipartition of forces[7] or numerical methods, such as finite element/volume modeling.[8–10] This article extends past Second Law advances to microfluidic energy conversion, particularly embedded microchannels adopted for flow control purposes.[11] The microprofiled surfaces will be optimized with respect to thermal and fluid friction irreversibilities of two-dimensional external flow, based on Blasius-type similarity solutions of boundary-layer flow.

The motivation of this study is to develop an alternative technique of drag reduction and heat-transfer enhancement by using optimized surface microgrooves, in contrast to past methods such as annular fins,[12] corrugated surfaces,[13] and other passive techniques in heat exchangers.[14] Slip-flow conditions within the embedded surface microchannels enable this drag reduction and boundary-layer control. Based on past Blasius-type similarity analysis,[15] a no-slip solution (outside of microchannels; $Kn < 0.001$) is combined with a slip-flow solution within the embedded microchannels ($0.02 < Kn < 0.07$). But in contrast to those past studies,[15] it is shown how slip-flow and no-slip configurations can be most effectively combined for purposes of reducing entropy production in convective heat-transfer problems.

II. Convective Heat-Transfer and Boundary-Layer Flow

The flow configuration is depicted in Fig. 1. Convective heat transfer and boundary-layer flow along a flat surface are predicted with a similarity solution. The predicted velocity u is expressed in terms of a similarity variable ξ, freestream velocity u_∞, and stream function derivative as follows[14]:

$$u/u_\infty = f'(\xi) \tag{1}$$

where

$$\xi = z\sqrt{u_\infty/\nu x} \tag{2}$$

The unknown stream function $f(\xi)$ is determined from the following Blasius equation of momentum transport within the boundary layer:

$$f'''(\xi) + \tfrac{1}{2} f(\xi) f''(\xi) = 0 \tag{3}$$

This third-order nonlinear differential equation is solved with a Runge–Kutta method, subject to boundary conditions of $f'(\infty) = 1$, $f(0) = 0$, and a no-slip condition at the wall, $f'(0) = 0$.

Within the interspersed open microchannels along the wall, slip-flow behavior at higher Knudsen numbers requires that the wall boundary condition is replaced by the following slip-flow condition[16]

$$u(0) = \left(\frac{2-\sigma}{\sigma}\right)\lambda \left.\frac{\partial u}{\partial z}\right|_0 \tag{4}$$

where σ and λ refer to the tangential momentum accommodation coefficient and mean free path, respectively. In terms of similarity variables, the slip-flow condition can be expressed as

$$f'(0) = K_1 f''(0) \tag{5}$$

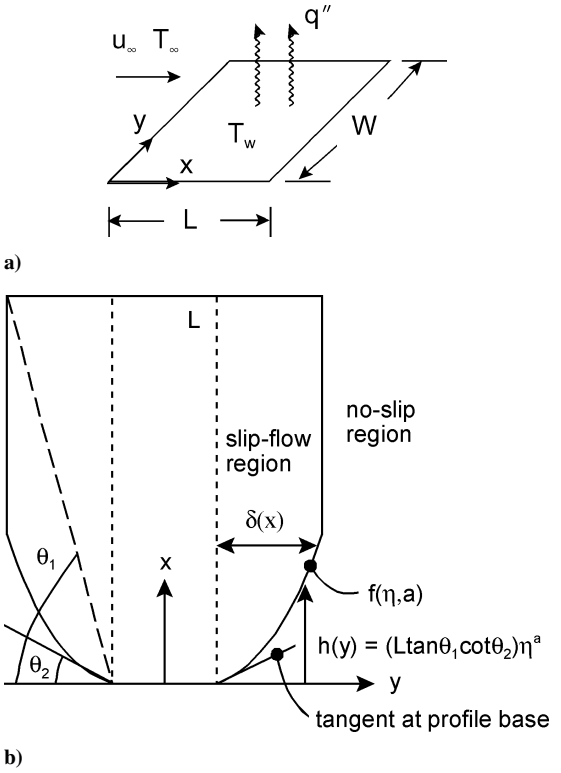

Fig. 1 Schematic of a) external flow and b) geometric profile of an open microchannel (embedded in the surface, parallel to others in the *x* direction).

where

$$K_1 = [(2-\sigma)/\sigma] Kn_x Re_x^{\frac{1}{2}} \tag{6}$$

and Kn_x and Re_x refer to the local Knudsen number (ratio of the mean free path to a characteristic length scale of the microchannel) and Reynolds number, respectively.

After solving the boundary-layer equation with a slip-flow boundary condition, the resulting wall shear stress and convective heat transfer depend on the slip coefficient. For both cases of slip-flow and no-slip (without microchannels), the following correlations are approximated at Prandtl numbers close to 1:

$$\tau_w \big/ \rho u_\infty^2 = f''(0) \cdot Re_x^{-\frac{1}{2}} \tag{7}$$

$$Nu_x = hx/k = \theta'(0) \cdot Re_x^{\frac{1}{2}} \tag{8}$$

For no-slip conditions, $f''(0) = 0.3321$, but $f''(0)$ varies with K_1 for the slip-flow problem, that is,

$$f''(0) = \frac{1.39}{4.185 + 0.96 K_1^{1.11}} \tag{9}$$

This nondimensional expression is also approximated for the nondimensional temperature gradient at the wall, when applied to the previous convective heat-transfer analysis.

III. Entropy Production for Microprofiled Surfaces

The total entropy production over a plate of length L and a width of W is[14]

$$\dot{S}_{\text{gen}} = \left(\frac{q''}{T_\infty}\right)^2 \int_0^W \int_0^L \frac{dx\,dy}{h} + \frac{u_\infty}{T_\infty} \int_0^W \int_0^L \tau_w \, dx\, dy \tag{10}$$

The preceding correlations for the convection coefficient (based on the Nusselt number) and wall shear stress are substituted into this equation. In this section, the entropy production will be analyzed for the following three cases: 1) diverging/converging embedded

microchannels, 2) unspecified (exponential) profile of microchannels, and 3) unspecified cross-stream variation of the microchannel geometrical profile.

A. Case 1) Diverging/Converging Microchannels, Laminar Flow, Uniform Wall Heat Flux

For diverging (or converging) microchannels, the predicted entropy production involves a parallel section and varying slip-slip areas. It can be shown that the total entropy production over the plate becomes

$$\dot{S}_{\text{gen}} = \left(\frac{q''^2\nu^2}{kT_\infty^2 u_\infty^2}\right)\left\{n\int_0^{Re_L}\int_0^{W_s+2d}\frac{Re_x^{\frac{1}{2}}}{\theta_s'(0)}\,\mathrm{d}y\,\mathrm{d}Re_x + \int_0^{Re_L}\int_0^{W-nW_s}\frac{Re_x^{\frac{1}{2}}}{\theta_{\text{ns}}'(0)}\,\mathrm{d}y\,\mathrm{d}Re_x\right\} + \left(\frac{u_\infty^2\mu}{T_\infty}\right)\left\{n\int_0^{Re_L}\int_0^{W_s+2d}\frac{f_s''(0)}{Re_x^{\frac{1}{2}}}\,\mathrm{d}y\,\mathrm{d}Re_x + \int_0^{Re_L}\int_0^{W-nW_s}\frac{f_s''(0)}{Re_x^{\frac{1}{2}}}\,\mathrm{d}y\,\mathrm{d}Re_x\right\} + \dot{S}_{\text{gen},f} + \dot{S}_{\text{gen},h} \tag{11}$$

where the subscripts s and ns refer to slip-flow and no-slip regions, respectively. In this result, the latter two integrals, $\dot{S}_{\text{gen},f}$ and $\dot{S}_{\text{gen},h}$, refer to the wall friction irreversibility difference and wall thermal irreversibility difference caused by slip minus no-slip conditions, that is,

$$\dot{S}_{\text{gen},h} = \left(\frac{q''^2\nu^2}{kT_\infty^2 u_\infty^2}\right)2n\int_0^{Re_L}\int_0^{\delta}\left[\frac{Re_x^{\frac{1}{2}}}{\theta_s'(0)} - \frac{Re_x^{\frac{1}{2}}}{\theta_{\text{ns}}'(0)}\right]\mathrm{d}y\,\mathrm{d}Re_x \tag{12}$$

$$\dot{S}_{\text{gen},f} = \left(\frac{u_\infty^2\mu}{T_\infty}\right)2n\int_0^{Re_L}\int_0^{\delta}\left[\frac{f_s''(0)}{Re_x^{\frac{1}{2}}} - \frac{f_{\text{ns}}''(0)}{Re_x^{\frac{1}{2}}}\right]\mathrm{d}y\,\mathrm{d}Re_x \tag{13}$$

It can be shown that the total entropy production over the plate becomes a sum of entropy production rates for parallel microchannels (subscript p) and irreversibility difference integrals for diverging/converging microchannels ($\dot{S}_{\text{gen},f}$ plus $\dot{S}_{\text{gen},h}$), that is,

$$\dot{S}_{\text{gen}} = \dot{S}_{\text{gen},p} + \dot{S}_{\text{gen},h} + \dot{S}_{\text{gen},f} \tag{14}$$

This result applies to diverging microchannels. An analogous result is obtained for converging microchannels, after subtracting the latter two terms (rather than adding the terms). Without these latter two terms, the result represents the entropy generation over a surface with interspersed parallel microchannels.

B. Case 2) Unspecified (Exponential) Profile, Laminar Flow, Uniform Wall Heat Flux

Consider a practical case where the best geometrical profile of embedded microchannels is unknown (or unspecified). The profile is characterized by an unknown function $h(y)$, which is determined based on minimization of entropy production along the microprofiled plate. The procedure of establishing the optimal profile is called entropy-based surface microprofiling (EBSM).

Define a nondimensional profile variable as follows:

$$\eta = y/L\cot\theta_2, \qquad 0 \le n \le 1 \tag{15}$$

The varying distance between the microchannel base and edge point (see Fig. 1) becomes

$$h = (L\tan\theta_1\cot\theta_2)\eta \tag{16}$$

An exponentially varying profile shape is defined by

$$h = (L\tan\theta_1\cot\theta_2)\eta^a \tag{17}$$

From this definition, it is required that $h(0)=0$ and $h(1)=L\tan(\theta_1)\cot(\theta_2)$.

In terms of these variables, the thermal irreversibility difference integral becomes

$$\dot{S}_{\text{gen},h} = \left(\frac{q''^2\nu^{\frac{1}{2}}}{kT_\infty^2 u_\infty^{\frac{1}{2}}}\right)2n\left[\frac{1}{\theta_s'(0)} - \frac{1}{\theta_{\text{ns}}'(0)}\right]\int_0^1\int_h^L L\cot\theta_2 x^{\frac{1}{2}}\,\mathrm{d}x\,\mathrm{d}\eta \tag{18}$$

Performing the integrations with the varying geometrical profile,

$$\dot{S}_{\text{gen},h} = \left(\frac{q'^2\nu}{kT_\infty^2 u_\infty}\right)0.921nK_1^{1.11} \times\left[\cot\theta_2 - \left(\frac{2}{3a+2}\right)\cot^{\frac{5}{2}}\theta_2\tan^{\frac{3}{2}}\theta_1\right]Re_L^{\frac{1}{2}} \tag{19}$$

Similarly, the friction irreversibility integral becomes

$$\dot{S}_{\text{gen},f} = \left(\frac{u_\infty^{\frac{5}{2}}\rho^{\frac{1}{2}}\mu^{\frac{1}{2}}}{T_\infty}\right)2n\left[f_s''(0) - f_{\text{ns}}''(0)\right] \times\int_0^1\int_h^L L\cot\theta_2 x^{-\frac{1}{2}}\,\mathrm{d}x\,\mathrm{d}\eta \tag{20}$$

which yields

$$\dot{S}_{\text{gen},f} = \left(\frac{u_\infty\mu^2}{\rho T_\infty}\right)\left(\frac{5.56}{4.185+0.96K_1^{1.11}} - 1.328\right)n \times\left[\cot\theta_2 - \left(\frac{2}{a+2}\right)\cot^{\frac{3}{2}}\theta_2\tan^{\frac{1}{2}}\theta_1\right]Re_L^{\frac{3}{2}} \tag{21}$$

It can be observed that the same result is obtained as the preceding case (embedded linearly converging/diverging microchannels), except that the factor $\frac{2}{5}$ is replaced by $2/(3a+2)$ in the thermal irreversibility integral. Also, $\frac{2}{3}$ is replaced by $2/(a+2)$ in the friction irreversibility integral. When a value of $a=1$ (linear profile) is substituted into these expressions, the generalized results match the special geometrical case for linearly converging/diverging microchannels.

The preceding irreversibility difference integrals are combined into the total entropy production over the plate (per unit width). Then, the optimal shape profile of the embedded microchannels can be obtained by differentiating that expression with respect to the profile parameter, a, and setting the result equal to zero. For a diverging profile,

$$6A/(3a+2)^2 + 2B/(a+2)^2 = 0 \tag{22}$$

where

$$A = \left(\frac{q'^2\nu}{\rho u_\infty T_\infty^2}\right)0.921nK_1^{1.11}\cot^{\frac{5}{2}}\theta_2\tan^{\frac{3}{2}}\theta_1 Re_L^{\frac{1}{2}} \tag{23}$$

$$B = \left(\frac{u_\infty\mu^2}{\rho T_\infty}\right)\left(\frac{5.56}{4.185+0.96K_1^{1.11}} - 1.328\right)n\cot^{\frac{3}{2}}\theta_2\tan^{\frac{1}{2}}\theta_1 Re_L^{\frac{3}{2}} \tag{24}$$

For a converging profile, a minus sign is placed before each expression for the coefficients A and B. Solving the preceding second-order algebraic equation for the optimal profile coefficient,

$$a = [2/(3A+9B)]\left[-3A-3B + \sqrt{9(A+B)^2 - 3(A+3B)(3A+B)}\right] \tag{25}$$

When substituted into the profile distribution for $h(y)$, the resulting shape of the embedded microchannels minimizes the entropy production over the plate.

C. Case 3) Unspecified Cross-Stream Profile Variation, Laminar Flow, Uniform Wall Heat Flux

Leaving out the integration of total entropy production in the y direction, the minimization of entropy production yields a detailed variation of microchannel profile in that direction. The thermal and friction irreversibility difference integrals become

$$\dot{S}_{\text{gen},h} = \left(\frac{q'^2}{kT_\infty^2}\right) 0.461 K_1^{1.11} \left[1 - f^{\frac{3}{2}}(a,\eta)\cot^{\frac{3}{2}}\theta_2 \tan^{\frac{3}{2}}\theta_1\right] Re_L^{-\frac{1}{2}} \tag{26}$$

$$\dot{S}_{\text{gen},f} = \left(\frac{u_\infty^2 \mu}{T_\infty}\right)\left[\frac{2.78}{4.185 + 0.96K_1^{1.11}} - 0.664\right] \times \left[1 - f^{\frac{1}{2}}(a,\eta)\cot^{\frac{1}{2}}\theta_2 \tan^{\frac{1}{2}}\theta_1\right] Re_L^{\frac{1}{2}} \tag{27}$$

Combining these irreversibility integrals with the portions arising from parallel embedded microchannels, the total entropy production over the plate becomes

$$\begin{aligned}\dot{S}_{\text{gen}} = \left(\frac{q'^2}{kT_\infty^2}\right) &\Big\{4.016 + 0.461 K_1^{1.11} \\ &+ 0.461 K_1^{1.11}\left[1 - f^{\frac{3}{2}}(a,\eta)\cot^{\frac{3}{2}}\theta_2 \tan^{\frac{3}{2}}\theta_1\right]\Big\} Re_L^{-\frac{1}{2}} \\ &+ \left(\frac{u_\infty^2 \mu}{T_\infty}\right)\left\{\frac{2.78}{4.185 + 0.96K_1^{1.11}} + 0.664 \right. \\ &+ \left(\frac{2.78}{4.185 + 0.96K_1^{1.11}} - 0.664\right) \\ &\left. \times \left[1 - f^{\frac{1}{2}}(a,\eta)\cot^{\frac{1}{2}}\theta_2 \tan^{\frac{1}{2}}\theta_1\right]\right\} Re_L^{\frac{1}{2}}\end{aligned} \tag{28}$$

The first, second, fourth, and fifth terms represent the irreversibility contributions from the parallel microchannel profile. The remaining third and sixth terms, involving the trigonometric factors, represent the contributions arising from profile corrections (caused by deviations of profile width in the streamwise direction).

Unlike exponential profiles documented previously, Spivey and Tortorelli[17] have used cubic splines for optimizing the geometry of a rigid surface, particularly with applications to nonlinear contact problems for beams. The cubic splines are parameterized by a series of control points that serve as the design parameters for the optimization problem. When using cubic splines for interpolation, a set of piecewise third-order polynomials is fitted through the set of control points. The second derivative of each polynomial is usually set to zero at the endpoints, thereby providing boundary conditions that complete the system of equations. These equations are solved to give the coefficients of the polynomials. This method effectively fits a cubic function through a given control point and one point on either side of it. A useful advantage of the method is that it gives an exact curve fit without spurious oscillations.

But a cubic spline algorithm is considered to be much slower than direct interpolations used in this paper. In the current formulation, fitting coefficients can be determined analytically, whereas multiple cubic splines would require numerical solutions of a set of discrete algebraic equations. For cubic splines, each curve is constrained to pass through all of the points, while requiring the first and second derivatives to be the same on either side of the center point. These constraints are not considered to be necessary for the relatively basic converging and diverging profile geometries in this article. However, cubic splines provide a very useful approach for extensions of the current algorithm to more complex geometrical configurations.

IV. Results and Discussion

Numerical results for air (300 K) are presented in this section. In Fig. 2, the change of optimized profile parameter, a, at varying Reynolds numbers, wall heat fluxes, and slip coefficients is presented. Geometrical and surface parameters are shown in the figure. Each profile parameter minimizes the combined entropy production of thermal and friction irreversibilities under each set of flow conditions. This parameter affects the relative proportion of surface area containing slip-flow and no-slip conditions. The friction irreversibility increases for larger surface areas exposed to no-slip conditions, as a result of added surface friction. But the thermal irreversibility decreases because a smaller temperature difference (between the wall and surrounding fluid) is needed to transfer a fixed rate of heat flow q'. Slip-flow conditions within the embedded microchannels lead to lower friction irreversibility, but only over a certain range of conditions because they contribute simultaneously to additional surface area with friction.

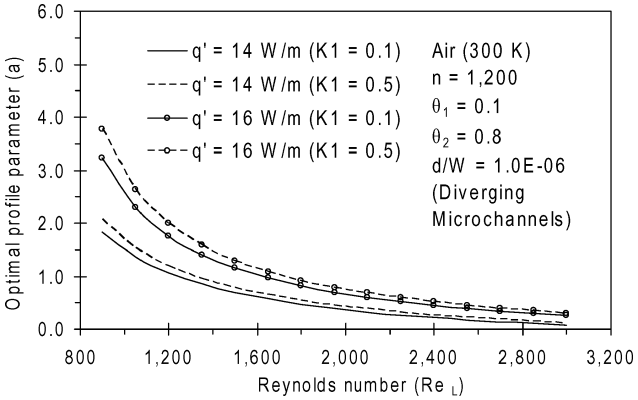

Fig. 2 Change of optimized profile parameter with Reynolds number.

Slip-flow conditions entail direct momentum exchange of intermolecular interactions near the wall. The probability of a fluid molecule striking another fluid molecule within an embedded microchannel, rather than a wall, decreases at higher Knudsen numbers. In results outlined in this section, the Knudsen number varies between about 0.02 and 0.07. These values fall within $0.001 < Kn < 0.1$, which represents the range governed by the Navier–Stokes equations with slip-flow boundary conditions.[16] A molecule can reflect from several walls before colliding with another fluid molecule traveling in the principle flow direction. Some molecules reflect specularly, and other molecules reflect diffusely from the surface of the walls. Thus, a portion of momentum of incident molecules is lost to the wall, while the remaining portion is retained by the reflected molecules. The tangential momentum accommodation coefficient is used to represent the fraction of incident molecules that are reflected diffusely. This coefficient typically varies between 0.2 and 0.8 (Ref. 16) and depends on the fluid properties, solid wall, and the surface finish.

For an idealized smooth wall, the incident angle exactly matches the reflected angle of impacting molecules. The molecules conserve tangential momentum, thereby not exerting shear on the wall. This process of specular reflection leads to perfect slip at the wall. But for an actual wall with surface roughness, the molecules reflect at some random angle, which is uncorrelated with their incident angle. Perfectly diffuse reflection requires zero tangential momentum for the reflected fluid molecules to be balanced by a finite slip velocity, to account for the shear stress transmitted to the wall. A near-wall force balance requires that the difference between the slip velocity and wall velocity balances the product of mean free path and velocity gradient perpendicular to the wall. This balance has been applied as the slip-flow boundary condition in the previous similarity solution of boundary-layer flow. Slip occurs only when the mean velocity of molecules changes significantly over a distance of about one mean free path.

In Fig. 2, the optimized surface profile parameter decreases at higher Reynolds numbers. At a fixed freestream velocity, the surface area increases at higher Reynolds numbers. Also, smaller profile parameters lead to a decreasing slip-flow area. At higher Reynolds numbers, the minimal entropy production moves to lower values

of the profile parameter. The friction irreversibility rises earlier at those lower values because of larger surface area. Also, Fig. 2 shows that the profile parameter increases at higher wall heat fluxes. More slip-flow area is needed to overcome added thermal irreversibility at those higher heat fluxes.

Similar trends are observed in Fig. 3, as the profile parameter decreases at higher Reynolds numbers. In this case, the surface heat flux (40 W/m) is fixed, but the base expansion angle varies between about 0.3 and 0.7 radians. When the base expansion angle increases, a larger proportion of no-slip area covers the surface. As a result, additional slip-flow area with a smaller profile parameter is needed to offset this change and minimize the entropy production. The predicted results approach a certain constant value asymptotically at high base expansion angles. The profile parameter becomes nearly independent of base angle when the geometrical configuration approaches the case of parallel embedded microchannels.

For the third case of an unspecified cross-stream profile, the entropy production varies spatially (i.e., changes with x and η) across each microchannel. These spatial variations are depicted in Fig. 4 for a linearly diverging microchannel ($a = 1$), as well as second-order ($a = 2$), third-order ($a = 3$), and fourth-order ($a = 4$) profiles. Airflow at 300 K and specified values of slip coefficient (0.06), Reynolds number (3×10^5), and the number of embedded microchannels (2200) are considered. At a specified position η, less entropy production occurs with the embedded microchannels because of lower friction irreversibility of slip-flow conditions. The entropy production increases at higher values of η, when the slip-flow area decreases and friction irreversibilities rise. Also, a constant value of entropy production is predicted for the case without microchannels, as a result of no-slip conditions across the plate in the η direction.

The entropy generation decreases for higher-order profiles in Fig. 4, as a result of larger slip-flow area and reduced friction irreversibility. Similar observations have been reported previously by Fabbri[18] in regards to optimized thermal performance of finned surfaces. A genetic algorithm was applied to an extended surface fin with a polynomial geometrical profile. The polynomial parameters were selected for optimal fin effectiveness, similarly to parameters selected in Figs. 2 and 3 for minimal entropy production. But unlike Fabbri's thermal analysis[18] with a finite element method, this paper establishes the optimal profile coefficients analytically.

Figure 5 shows predicted trends of entropy production over a range of Reynolds numbers. The benchmark solution refers to the asymptotic no-slip limit, when correlations for the Blasius similarity solution can be integrated directly to yield the net entropy production (as documented in Ref. 14). This case without microchannels represents classical boundary-layer flow and convective heat transfer from a flat nonprofiled surface. It can be observed that the current numerical slip-flow formulation approaches this benchmark solution properly in the no-slip limit, when the slip coefficient becomes $K1 = 0$. The close agreement between predicted and benchmark results provides useful validation of the numerical modeling. Airflow at 300 K with 2800 parallel microchannels and a surface heat-transfer rate of 50 W/m is considered in Fig. 5.

Furthermore, experimental data have been reported by Czarske et al.[19] regarding wall shear stresses in the friction irreversibility portion of total entropy production. These data represent measured changes of skin-friction coefficients at varying Reynolds numbers in the no-slip limit case. In Fig. 5, these measured data (filled circle markers) are used for comparisons against the numerical modeling (solid line) and benchmark data (open-circle markers) in the no-slip limit case. Close agreement is also reached in these comparisons, thereby providing additional useful evidence regarding the current model's reliability.

The entropy production increases at low Reynolds numbers, when the smaller surface area leads to a high thermal irreversibility. When the surface area decreases, a larger temperature difference (between

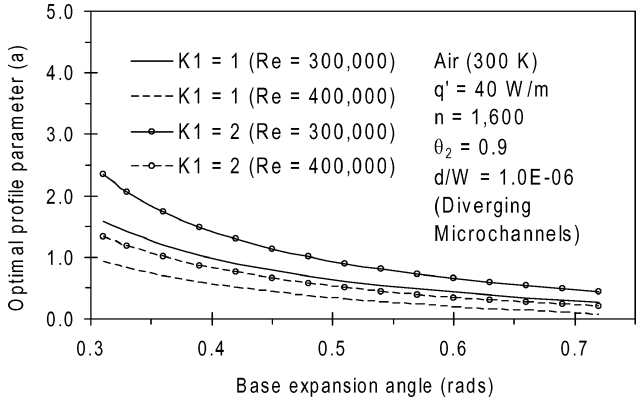

Fig. 3 Sensitivity to base expansion angle (diverging microchannels).

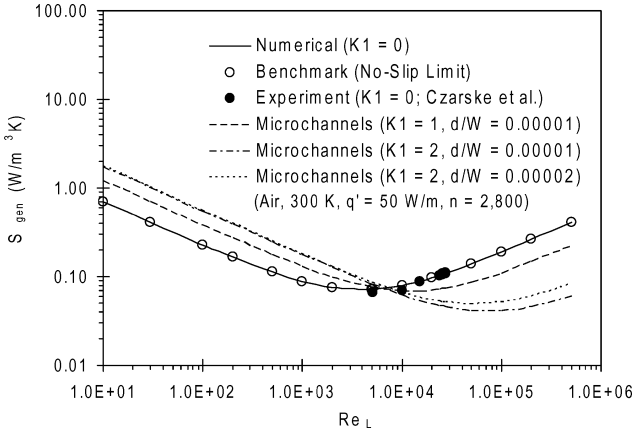

Fig. 5 Reduced entropy production with embedded surface microchannels.

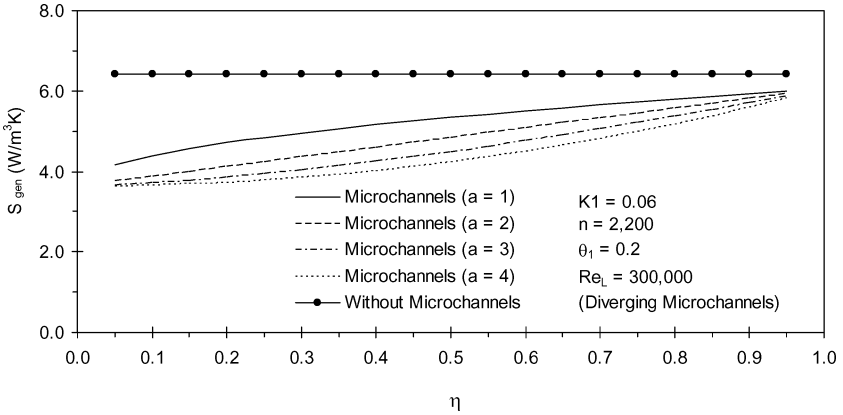

Fig. 4 Spatial variation of entropy generation.

the wall and surrounding fluid) is needed to transfer a fixed rate of heat transfer from the wall q'. On the other hand, friction irreversibilities increase at higher Reynolds numbers, as a result of more friction over a larger surface area. Thus, an optimal Reynolds number is predicted at a certain intermediate range, where the entropy production rate is minimized.

The predicted results show that the embedded microchannels allow lower values than the minimum entropy production without microchannels, because of slip-flow conditions within the microchannels. As a result, the adaptive microprofiling appears to provide a useful new technique of reducing entropy production in external flows. In Fig. 5, this entropy production decreases at higher slip coefficients and shallower microchannels. Drag reduction occurs at the higher slip coefficients, whereas less microchannel depth reduces the friction irrevresbility, as a result of less overall surface area.

In Fig. 5, it can be observed that the plate without embedded microchannels exhibits the lowest entropy production up to the critical Reynolds number. But this trend changes appreciably at larger Reynolds numbers. When the plate length and surface area become larger, the thermal irreversibility decreases and added area leads to greater surface friction. The resulting entropy production becomes lower for cases with microchannels, because the added friction irreversibility is more noticeably reduced by slip-flow conditions when the surface area increases. It seems that the beneficial impact of drag reduction by slip-flow conditions is not noticeable at lower Reynolds numbers, as thermal irreversibilities constitute a larger portion of the total entropy production. Additional surface area of embedded microchannels appears to raise friction irreversibilities more than frictional reduction by slip-flow conditions.

When analyzing the external flow conditions in these problems, the Reynolds number is characterized by the streamwise coordinate x and plate length L. In this paper, all geometrical and external flow parameters are selected to ensure that the Reynolds number remains below the point of transition to turbulence at $Re_L = 5 \times 10^5$. The formulation could be extended to external turbulent flows, provided that turbulence equations are supplied for the convective heat-transfer and wall-friction correlations.

On the other hand, the open microchannel flow depends on the microchannel depth (or hydraulic diameter) because similarities exist with closed microchannel flows. In this case, transition to turbulence occurs at Reynolds numbers of about 1.8×10^3. Sharp and Adrian[20] confirmed this transition point, after performing more than 1500 measurements of pressure drop and flow rate in microtubes. Microtube transition to turbulence is considered to have close similarities with rectangular channels having the same hydraulic diameter. The transition to turbulence was estimated when pressure drops exceeded macroscopic Poiseuille flow results for laminar flow resistance. Also, micro-PIV measurements of mean velocity and rms velocity fluctuations at the centerline were monitored at the transition point. Experimental uncertainties of $\pm 1\%$ systematic and $\pm 2.5\%$ rms random errors were reported by the authors.[20]

Based on microchannel depths and external flow velocities studied in this paper, the Reynolds numbers are well below the transition point of 1.8×10^3. Furthermore, the velocity required in the Reynolds number is best represented by the velocity at the top of the open microchannel (not the freestream velocity). Because this corresponds to the base of the boundary layer in external flow, it is approximately equal to the slip-flow velocity at the wall. At low-slip coefficients, this becomes much smaller than the freestream velocity. For example, the similarity solution of $f'(0)$ suggests that the wall velocity is about 0.02% of the freestream velocity at $K_1 = 0.3$. This produces much lower estimates of the microchannel Reynolds number, as compared with the freestream velocity. Thus, the microchannel flow is considered to be fully laminar.

In Fig. 6, the ratio of actual entropy production to the minimum entropy production (called the entropy generation number N_s) is plotted at varying length ratios L/L_{opt} and expansion angles of the microchannels. Linearly converging microchannels and airflow at 300 K are considered. Other problem parameters are depicted in Fig. 6. For small surface areas (low values of L/L_{opt}), the net entropy production occurs mainly from the thermal irreversibility.

The varying expansion angles appear to have minor effects on N_s at low values of L/L_{opt}, as those characteristics mainly affect the friction irreversibilities. On the other hand, the slip-flow friction irreversibilities rise faster than the no-slip case for all of the expansion angles in Fig. 6. For a specified surface length, the entropy production increases faster at smaller base and exit expansion angles, relative to the corresponding minimum entropy production, which decreases with added slip-flow area.

Unlike Figs. 2 and 3 (diverging microchannels), the predicted results in Figs. 7 and 8 consider converging microchannels. The same angles of Fig. 1 are used, but the microchannel converges into the central parallel section, rather than expanding outwards from it. On the vertical axis of Fig. 7, the slip-flow area decreases at lower values of the profile parameter. For example, because the geometrical configuration represents converging microchannels, the slip-flow area at $a = -0.7$ exceeds the slip-flow area at $a = -0.6$. In Fig. 7, the profile parameter decreases at higher slip coefficients. A higher slip coefficient overcomes the added friction irreversibility of less slip-flow area. Also, the profile parameter decreases at lower Reynolds numbers, which also entails reduced friction irreversibilities with a smaller surface area.

Similar trends are observed in Fig. 8, where the profile parameter decreases at higher slip coefficients and lower Reynolds numbers. In Fig. 8, airflow at 300 K is considered with specified values of the surface heat-transfer rate (100 W/m) and base contraction angle (0.2 rads). Other flow and surface parameters are illustrated in Fig. 8. The profile parameter increases (larger slip-flow area) in order to overcome the reduced slip-flow area at higher exit contraction

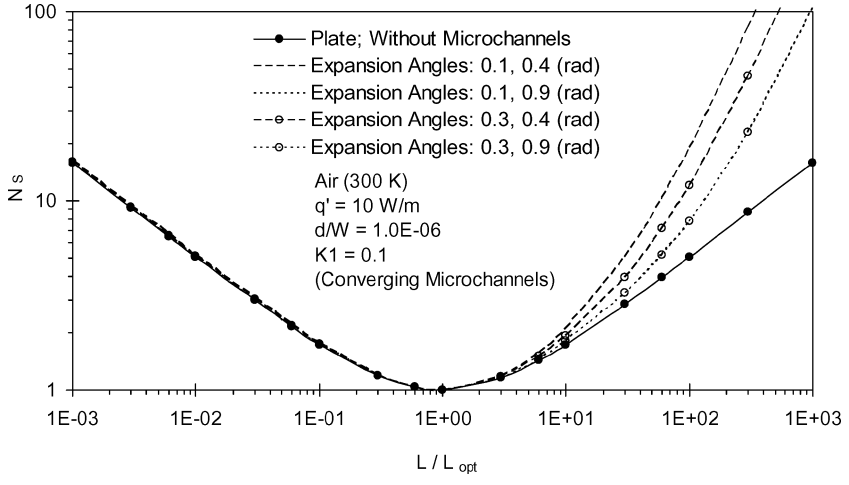

Fig. 6 Comparison of predicted entropy generation number with benchmark result.

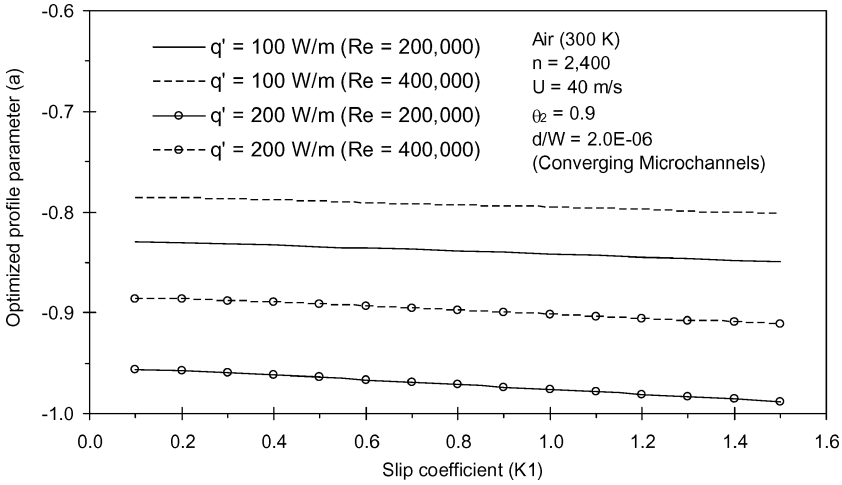

Fig. 7 Sensitivity to slip coefficient (converging microchannels).

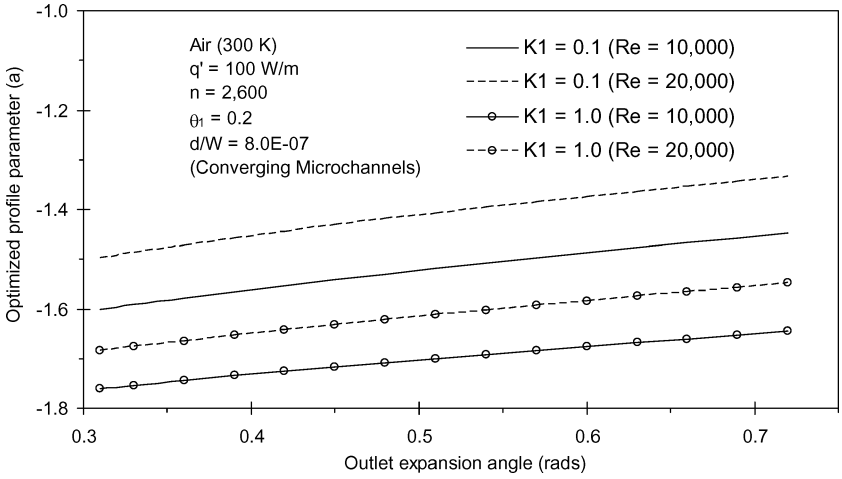

Fig. 8 Sensitivity to outlet expansion angle (converging microchannels).

angles. The optimized profile parameter reflects the desired geometrical configuration of converging microchannels, which minimizes the net entropy production over the surface as a result of combined thermal and friction irreversibilities.

The corners of the embedded microchannels represent a transition connecting the no-slip regime (above microchannel; $Kn < 0.001$) and slip-flow regime (within a microchannel; $0.001 < Kn < 0.1$). When calculating the local Knudsen number, the corresponding length scale must accommodate both microchannel depth and width or a hydraulic diameter-based length. Otherwise, no-slip conditions could be erroneously predicted near the corners. For example, a wide microchannel with a submicron or nanoscale depth could produce an unrealistic Knudsen number if the width alone were used. It is anticipated that the local Knudsen number decreases below 0.001 and moves into the no-slip regime at some point near the top corner. This arises with diminished effects of side walls on the intermolecular interactions near the corners. This transition to no-slip conditions is considered to produce a small submicron semicylindrical type zone of influence at the top corners. This zone penetrates mainly into the open microchannel, as fully no-slip conditions are expected outside of the microchannels.

To the author's knowledge, little or no experimental data have been reported previously regarding such transition from slip-flow to no-slip behavior near the corners of open microchannels. It would be interesting to observe whether transition-induced variations of the slip-flow coefficient could be estimated from measured mass-flow rate changes at varying pressure differences and microchannel depths in a controlled experiment. But such studies can only suggest a single (net) coefficient, without spatial variations across the microchannel. In this paper, the spatial variation is represented by a single effective slip coefficient, which approximates the same wall friction as the actual case with varying slip coefficients. This effective coefficient accommodates an averaged slip coefficient over the transition region.

V. Conclusions

This paper develops a new technique of adaptively optimized microgrooves in a surface, with geometrical profiles selected to minimize entropy production over the surface. Drag reduction of slip-flow conditions within microchannels overcomes the friction irreversibility of added surface area. A profile parameter characterizes the optimized geometrical configuration of each embedded microchannel. For diverging microchannels, this parameter decreases at higher Reynolds numbers and lower wall heat fluxes. For airflow at 300 K with 1600 microchannels, the parameter decreases at higher exit expansion angles. The spatial variation of entropy production in the cross-stream direction shows that lower entropy production occurs near the centerline of the microchannel. For airflow at 300 K, the minimum entropy production decreases for shallower embedded microchannel depths and higher slip coefficients. Also, the entropy generation number increases at smaller base and exit expansion angles for converging microchannels. By establishing microprofiled surfaces with minimum entropy production, lower system input power is needed to transfer fluid across the surface at specified rates of mass and heat flow.

Acknowledgments

Support of this microsystems research from Western Economic Diversification, Westland Helicopters Ltd., Canada Foundation for Innovation, and the Natural Sciences and Engineering Research Council of Canada is gratefully acknowledged.

References

[1]Sammarco, T. S., and Burns, M. A., "Thermocapillary Pumping of Discrete Drops in Microfabricated Analysis Devices," *AIChE Journal*, Vol. 45, 1999, pp. 350–366.

[2]Kataoka, D. E., and Troian, S. M., "Patterning Liquid Flow on the Microscopic Scale," *Nature*, Vol. 402, 1999, pp. 794–797.

[3]Raju, R., and Roy, S., "Modeling Single Component Transport Through Micro Channels and Free Molecule Micro-Resistojet," AIAA Paper 2004-1342, Jan. 2004.

[4]Lim, S., and Choi, H., "Optimal Shape Design of a Pressure Driven Curved Micro Channel," AIAA Paper 2004-624, Jan. 2004.

[5]Raju, R., and Roy, S., "Hydrodynamic Model for Microscale Flows in a Channel with Two 90° Bends," *Journal of Fluids Engineering*, Vol. 126, No. 3, 2004.

[6]Dincer, I., and Rosen, M. A., "Exergy Efficiencies of Sensible, Mixed Thermal Energy Storage Systems," ASHRAE Paper 4393, June 2000.

[7]Nummedal, L., and Kjelstrup, S., "Equipartition of Forces as a Lower Bound on the Entropy Production in Heat Exchange," *International Journal of Heat and Mass Transfer*, Vol. 44, No. 15, 2001, pp. 2827–2833.

[8]Naterer, G. F., "Constructing an Entropy-Stable Upwind Scheme for Compressible Fluid Flow Computations," *AIAA Journal*, Vol. 37, No. 3, 1999, pp. 303–312.

[9]Naterer, G. F., "Applying Heat—Entropy Analogies with Experimental Study of Interface Tracking in Phase Change Heat Transfer," *International Journal of Heat and Mass Transfer*, Vol. 44, No. 15, 2001, pp. 2917–2932.

[10]Naterer, G. F., and Camberos, J. A., "Entropy and the Second Law in Fluid Flow and Heat Transfer Simulation," *Journal of Thermophysics and Heat Transfer*, Vol. 17, No. 3, 2003, pp. 360–371.

[11]Naterer, G. F., Chomokovski, S. R., Friesen, C., and Shafai, C., "Micro-Machined Surface Channels Applied to Engine Intake Flow and Heat Transfer," AIAA Paper 2003-4054, June 2003.

[12]Antar, M. A., "Steady and Transient Numerical Analysis of the Performance of Annular Fins," *International Journal of Energy Research*, Vol. 25, No. 13, 2001, pp. 1197–1206.

[13]Zimparov, V., "Energy Conservation Through Heat Transfer Enhancement Techniques," *International Journal of Energy Research*, Vol. 26, No. 7, 2002, pp. 675–696.

[14]Naterer, G. F., *Heat Transfer in Single and Multiphase Systems*, CRC Press, Boca Raton, FL, 2002.

[15]Martin, M. J., and Boyd, I. D., "Blasius Boundary Layer Solution with Slip Flow Conditions," *Rarefied Gas Dynamics*, edited by T. J. Bartel and M. A. Gallis, Sydney, 2001.

[16]Gad-el-Hak, M., "The Fluid Mechanics of Microdevices—The Freeman Scholar Lecture," *ASME Journal of Fluids Engineering*, Vol. 121, 1999, pp. 5–33.

[17]Spivey, C. O., and Tortorelli, D. A., "Tangent Operators, Sensitivity Expressions and Optimal Design of Nonlinear Elastica in Contact with Applications to Beams," *International Journal for Numerical Methods in Engineering*, Vol. 37, 1994, pp. 49–73.

[18]Fabbri, G., "A Genetic Algorithm for Fin Profile Optimization," *International Journal of Heat and Mass Transfer*, Vol. 40, No. 9, 1997, pp. 2165–2172.

[19]Czarske, J., Buttner, L., Razik, T., Muller, H., Dopheide, D., Becker, S., and Durst, F., "Spatial Resolved Velocity Measurements of Shear Flows with a Novel Differential Doppler Velocity Profile Sensor," 11th International Symposium on Applications of Laser Techniques to Fluid Mechanics, July 2002.

[20]Sharp, K. V., and Adrian, R. J., "Transition from Laminar to Turbulent Flow in Liquid Filled Microtubes," *Experiments in Fluids*, Vol. 36, No. 5, 2004, pp. 741–747.